Effect of printing process parameters on tensile strength and wear rate of 17-4PH stainless steel deposited using SLM process

Priya Sahadevan
Lincoln University College, Selangor - 47301, Malaysia
priya@lincoln.edu.my, http://orcid.org/0009-0001-8220-3076

Chithirai Pon Selvan
School of Science and Engineering, Curtin University, Dubai - 345031, United Arab Emirates,
pon.selvan@curtindubai.ac.ae, http://orcid.org/0000-0001-9294-3340

Avinash Lakshmikanthan
Nitte Meenakshi Institute of Technology, Bengaluru - 560064, Karnataka, India
avinash.l@nmit.ac.in, https://orcid.org/0000-0002-6454-2904

Amiya Bhaumik
Lincoln University College, Selangor - 47301, Malaysia
amiya@lincoln.edu.my, http://orcid.org/0000-0002-9188-2269

Agustin Flores Cuautle
Postgraduate Studies and Research Division- Technological Institute of Orizaba, 94320 Orizaba, Ver., Mexico
Mexican National Council for Science and Technology-CONACYT
jose.fc@orizaba.tecnm.mx, http://orcid.org/0000-0003-0468-4764

KEYWORDS. 17-4PH SS, Tensile strength, Fracture studies, SLM process, Super Ranking Concept.

Citation: Sahadevan, P., Pon Selvan, C., Lakshmikanthan, A., Bhaumik, A., Cuautle, A. F., Effect of printing process parameters on tensile strength and wear rate of 17-4PH Stainless Steel deposited using SLM process, Frattura ed Integrità Strutturale, 70 (2024) 157-176.

Received: 23.04.2024
Accepted: 02.07.2024
Published: 15.08.2024
Issue: 10.2024

INTRODUCTION

Precipitate-hardened (PH) steels are engineered materials widely used to fabricate structural parts suitable for automotive, medical, and aerospace applications [1-3]. The use of PH steels (15-5PH, PH-13-8 Mo, 17-4 PH, 17-7 PH, and PH-8 Mo) as structural parts are due to excellent hardness possess up to 49 HRc [4], weldability [4-5], wear resistance [6], corrosion resistance, less distortion [7]. PH steels offer 3-4 times higher strength than austenitic stainless steels, namely 304 or 316 [8]. In addition, PH steels exhibit reduced and better ductility during their service life of components [9-10]. Strength is an essential property for any structural applications, and selecting an appropriate processing route for fabricating parts economically is of industrial relevance.

Subtractive, formative and joining processes are widely used to fabricate structural parts made of PH steels [11-13]. Subtractive manufacturing removes materials to reveal parts, resulting in material wastage [14]. The defects, such as segregations, nonmetallic inclusions, and non-uniform grain size, limit the use of the casting processing route [15]. The defects in ingots limit the use of further processes, namely forging, rolling, welding and heat treatment processes that reduce productivity [16]. Additive manufacturing (AM) technologies possess significant advantages over conventional manufacturing routes, such as reduced number of operations and assembly parts [17], economical [18], ease of fabrication of complex geometry structures with different combinations of materials [19], less material waste (i.e., 97% material efficient) [20] and environment-friendly processing route [21]. AM technologies are the proven processing routes to fabricate parts, and selecting the best among the seven different routes is of industrial and economic relevance [22].

AM techniques are classified based on liquid (stereolithography, fused deposition modelling), solid (laminate object manufacturing) and powder (selective laser sintering, selective laser melting, binder jetting, electron beam melting) processing routes [23]. AM processes are evaluated based on technical and economic criteria for processability, machine, and materials [22]. AM techniques are evaluated for the early design stage's initial technical and economic feasibility screening [24]. Selective laser melting techniques are comparable to selective laser sintering and outperform other techniques in terms of printed parts' accuracy, strength, and ductility [24]. The SLM possess a 95% print success rate over 90% of SLS, which reduces production costs [24]. SLM is designed as a hybrid process after combining desirable casting features and powder metallurgy to build parts layer-by-layer [25]. The un-melted metal powders were recycled and reused, leading to a competitive waste management advantage with SLM [26]. The un-melt metal powders greatly impacted void formation [27]. Maintaining appropriate material composition with recycled metal powders led to material design complexity [25]. The laser remelting improved the wettability, density, surface finish [28], mechanical properties [29], and microstructure [30] of SLM parts. Removing unmelt metal powders during processing led to the formation of a thick oxide layer and deteriorating surface quality [31]. The additional processing cost with the remelting strategy (adding ½ volumetric energy input is required to get a better surface finish mechanical and microstructure properties) [32] hinders the extensive use of the laser remelting technique. Therefore, attempts are required to improve parts quality during the processing stages employed in the SLM technique.

Higher roughness on the print parts ensures surface irregularities (porosity on the surface and subsurface), which acts as a nucleation site for corrosion subjected to an aggressive environment [33]. Microstructure changes from fine to coarse grains resulted in reduced mechanical strength [34]. Porosity in SLM parts causes more corrosion rate, whereas they result in a negligible impact on strength [34]. On the contrary, internal porosity decreases significantly the strength of the AlSi10Mg SLM parts [35]. The appropriate values of hatch spacing (i.e., adjusting the distance between points) parameter reduce the un-melted defects in SLM parts [36]. The scan speed is adjusted with a change in point distance (PD) and exposure time (ED) using a ratio of PD/ET [37]. The major disadvantages of SLM technology are low build rate and build rate computation using the product of layer thickness, scan speed and hatch distance [36]. The layer thickness directly influences manufacturing lead time and is reduced by ~1.6 when varied from 45 to 75 μm [38]. Regardless of many experiments, the authors conclude that significant attention must be paid to overcome shortcomings such as higher surface roughness, voids or porosity, low relative density, strengths, hardness, and corrosion resistance. Table 1 details the author's set of several process variables of SLM techniques using OFAT and DOE-based methods. The optimized combination resulted in significant differences in the final built parts of mechanical and microstructure characteristics. The disadvantages observed from OFAT techniques are increased experimental trials with variables and levels resulting in energy waste (labour, material, equipment, time-consuming, etc.) [39], interaction among the factors is neglected during process analysis on output functions [40-41], does not predict outputs for the known set of inputs, which demand to perform experiments and get trapped at sub-optimal solutions [42]. DOE technique overcomes the shortcomings of the OFAT approach, resulting in better solutions [40]. DOE provides invaluable process insights into SLM techniques. However, the optimal conditions differed for different materials because a) different process variables were investigated, b) different melting temperatures,

physical and powder composition, and c) different experimental and optimization methods. Furthermore, not many research efforts have been conducted to analyze the individual responses (ultimate tensile strength and wear rate) and optimize simultaneously both properties.

Steel Material	Input variables analyzed					Outputs Analysed	Optimization	Ref.
	LP (W)	LT (μm)	SS (mm/s)	HD (μm)	Others			
SS304	200-300	50	300-500	120-160	Nil	Strain	OFAT	Wen et al. 2020 [43]
SS316L	120-240	30	500-800	50-75	Nil	RS	OFAT	Waqar et al. 2021[44]
	200-250	30	800	120	Nil	TS, H & GS	OFAT	Yin et al. 2021[45]
SS316L	100-300	30	400-875	90-120	Nil	TS, & H	OFAT	Hitzler et al. 2017[46]
Maraging	280	40	960	110	Nil	CR	OFAT	Khan et al. 2021[33]
H13	170	-	400	-	Nil	D, H & TS	OFAT	Ren et al. 2019[47]
316L	120-190	-	300-990	80-130	Nil	TS, H, & RS	OFAT	Kluczyński et al. 2020[48]
316L	150-300	-	700-1300	60-120	Nil	RD & SR	DOE-C	Deng et al. 2020[49]
316L	400	200	-	4-64	ET: 80-180 μs	RD & TS	OFAT	Liu et al. 2021[36]
316L	206-298	-	900-1300	75-105	Nil	H, D, & SR	DOE-T	Jiang et al. 2019[50]
Maraging	400	45-75	600-1500	-	Nil	H, D, TS, & SR	OFAT	de Souza et al. 2019[38]
316L	180-240	20-35	500-800	-	Nil	EC, TS, & SR	DOE-T	Li et al. 2021a[51]
17- 4 PH	48	30	300	50	Nil	TS & FS	OFAT	Yadollahi et al. 2017[52]
17-4 PH	48-49	30	300-350	50	Nil	TS, CS & H	OFAT	Mahmoudi et al. 2017[53]
17-4 PH	162-207	30	1000-1400	52-66	DF: 3 mm	RS, P, IR & B	DOE	Linares et al. 2022[54]
17-4 PH	195	40	750	100	BPT: 40 °C	MS	OAFT	Vunnam et al. 2019[55]
17-4 PH	200-350	30	-	70-110	PD: 70-110 μm	VED	DOE-T	Ozsoy et al. 2021[56]
17-4 PH	50	30	140	50	BW: 70 μm	H & MS	OFAT	Leo et al. 2019[57]
17-4 PH	38	30	140	70	Nil	H, CR & MS	OFAT	Garcia-Cabezon et al. 2022[58]
17-4 PH	80-100	30	960-1440	45	Nil	ED, RD, H, & CR	DOE-T	Kartikeya Sarma et al. 2023[59]

Table 1: Summary results of experimental investigation carried out on input-output of SLM process. OFAT: one-factor-at-a-time; DOE-C: Design of experiments - central composite design; DOE-T: DOE-Taguchi; LP: Laser power; SS: Scan speed; LT: Layer thickness; HD: Hatch distance; TS: tensile strength; GS: grain structure; H: hardness; RS: residual stress; SR: surface roughness; CR: Corrosion rate; RD: relative density; CS: Compression strength; IR: Intensity ratio; B: Bending; MS: Microstructure; VED: Volumetric energy density; PD: Point distance; BPT: Build plate temperature.

The work attempts to build 17-4 PH SS parts using the SLM technique. SLM technological parameters (LP, SS, and HD) were studied to analyze the wear rate and ultimate tensile strength. The DOE-Taguchi method is applied for the experimental plan and analysis of the parametric contribution with a statistical evaluation technique: Pareto Analysis of variance. The limitation of DOE-Taguchi in determining the single technological parametric conditions of the SLM process was addressed by conducting multiobjective optimization (super ranking concept). The optimized conditions are validated and recommended to industry personnel for reference.

MATERIALS AND METHODS

Using SLM technology, EOS GMBH gas-atomized 17-4ph stainless steel powder was employed for sample deposition. SEM analyzed the powder particles' morphology, while iso 13320:2020 determined particle size distribution (30 ± 5 µm). The particles displayed annular morphology with a uniform size distribution. Figs. 1(a) and 1(b) depicted gas-atomized particles at 200x and a micro-dendritic pattern in 17-4ph stainless steel, respectively. Fig. 1(c) showed EDAX analysis, indicating iron (71.70%) as the primary constituent, with chromium, nickel, copper, manganese, and trace elements detected.

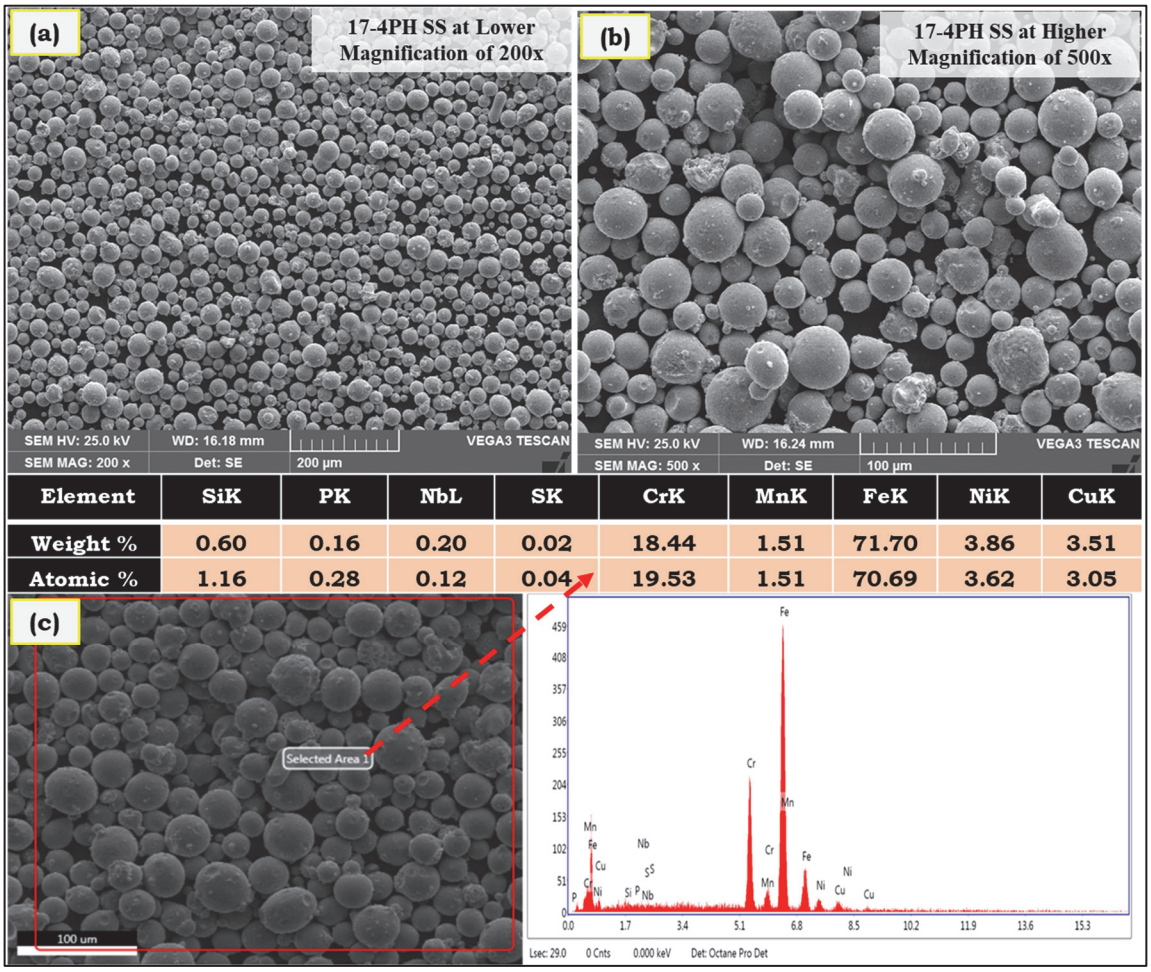

Element	SiK	PK	NbL	SK	CrK	MnK	FeK	NiK	CuK
Weight %	0.60	0.16	0.20	0.02	18.44	1.51	71.70	3.86	3.51
Atomic %	1.16	0.28	0.12	0.04	19.53	1.51	70.69	3.62	3.05

Figure 1: (a) and (b) Scanning electron micrographs of 17-4PH SS powders at lower and higher magnification; (c) EDAX analysis of 17-4PH SS powders using SEM.

The X-ray diffraction pattern of the Selective laser melted 17-4 PH steel sample has been indexed to α-fe, martensitic phase as indicated in the above figure. The respective hkl planes of (110), (200) and (211) indexed at 44.5, 65, and 82 degrees respectively denote α phase. In the present work as depicted in XRD peaks it's observed that the peak intensities are strong in BCC α-phase as shown in the figure.

EXPERIMENTAL METHOD

In the current experimental work, 17-4 precipitation-hardening stainless steel (PHSS) parts were deposited using Selective Laser Melting (SLM) having an average porosity of 0.0318%. This process is notable for its precision in fabricating metal parts directly from a 3D CAD model by melting metal powder layers using a high-energy laser beam. The experiment employs a Taguchi L9 orthogonal array to systematically study the effects of three SLM parameters at three

levels. Three SLM parameters are studied at three levels each based on our previous work [60-62] which implies the investigation focuses on optimizing these parameters to achieve the best possible material properties and surface finish of the 17-4 PHSS parts. Each experimental condition was repeated three times, ensuring reliability and statistical significance in the results.

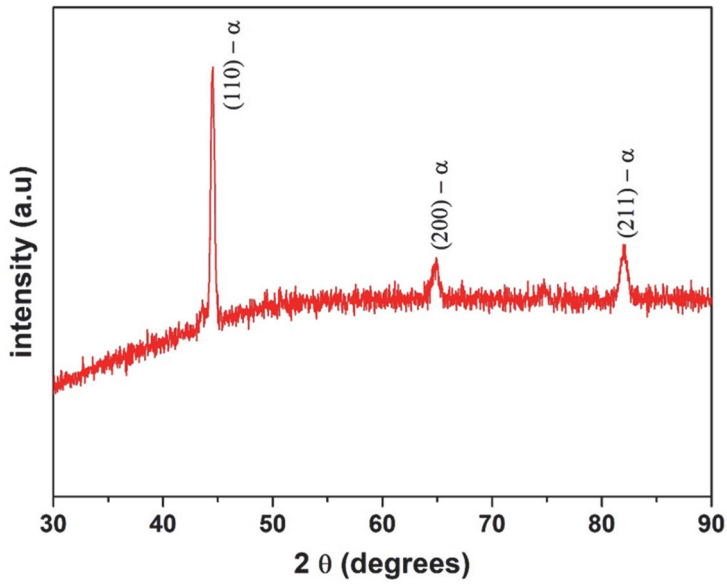

Figure 2: XRD pattern of 17-4PH SS-SLM Processed steel.

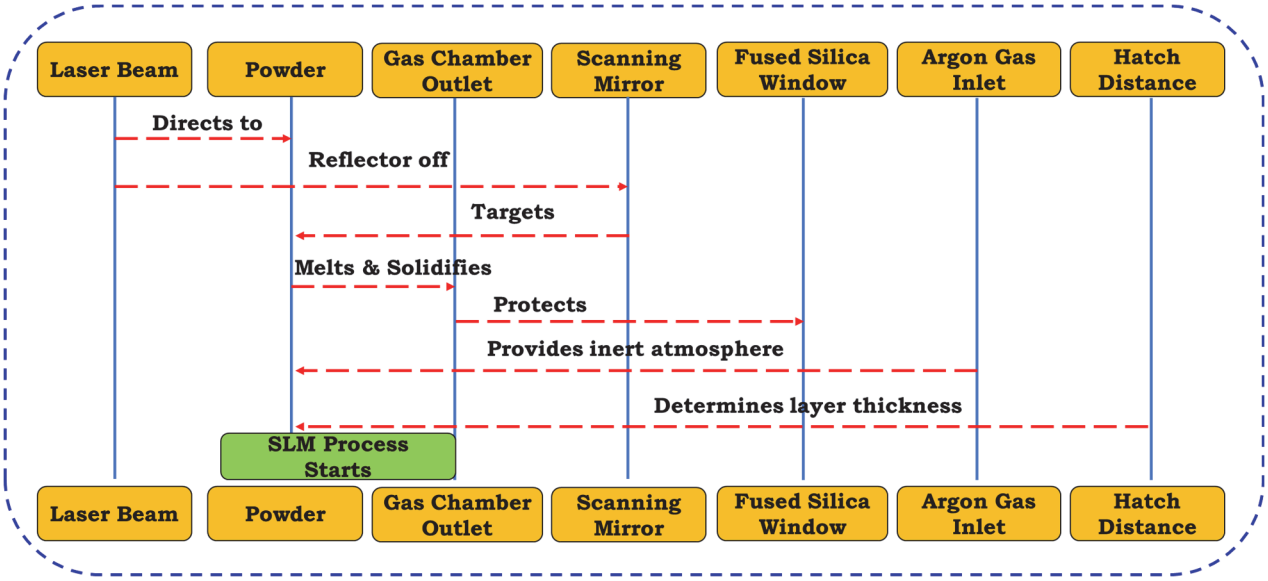

Figure 3: SLM process flowchart.

A fiber laser, operating at a wavelength of 1083 nm, equips the used SLM machine. The studies were conducted with a consistent laser spot size of around 100 µm, ensuring that the printed parts had precise and intricate details. The SLM procedure was carried out under a vacuum condition of $5e^{-6}$ MPa to avoid oxidizing of the samples. This controlled environment is crucial for maintaining the integrity and material properties of the parts. Argon gas (pressure $1e^{-6}$ MPa) was introduced during the experiments to study its effect on the build quality under different climatic conditions, which helps in improving the build quality and reducing defects. A detailed explanation is revealed in our previous work [62]. The SLM process is depicted as a flowchart in Fig. 3. This summary encapsulates the critical aspects of the SLM experimental setup for 17-4 PHSS parts fabrication, indicating a thorough and well-controlled approach to exploring the effects of various parameters on the printing process and resulting part quality. Fig. 4 depicts the sample dimensions and samples deposited using SLM process.

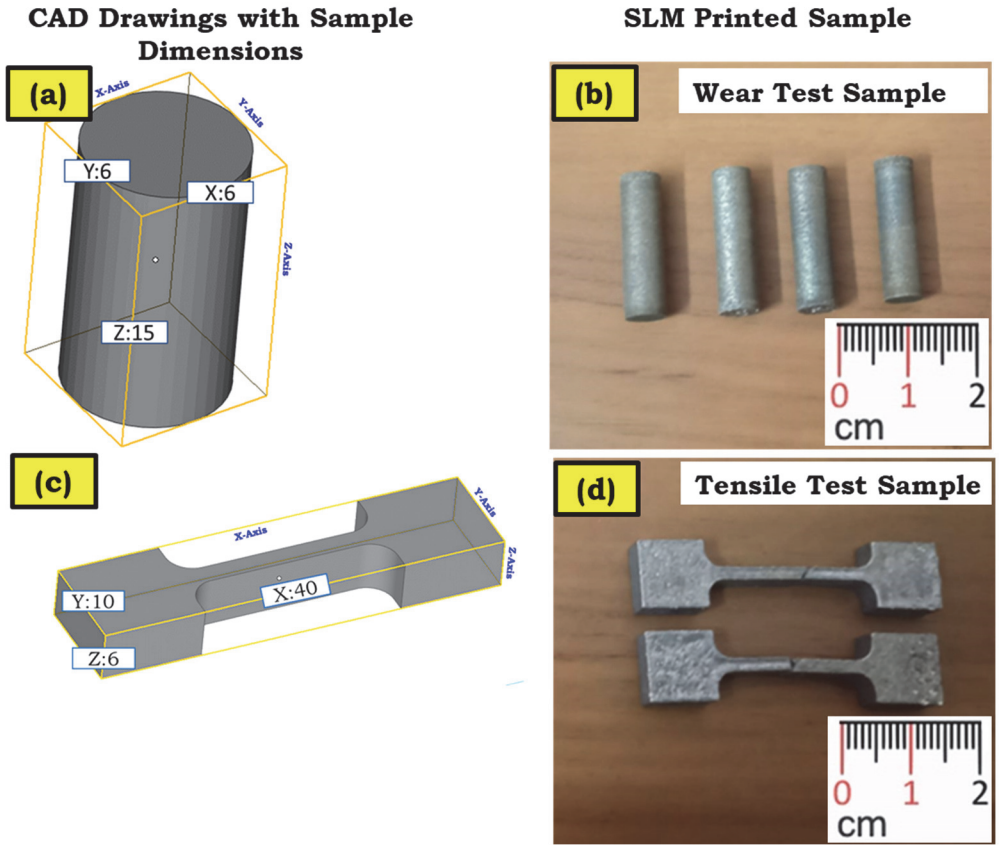

Figure 4: (a) and (c) Samples dimensions of wear and tensile test (b) and (d) 17-4PH SS wear and tensile test samples deposited during the SLM process.

RESPONSE MEASUREMENTS

To thoroughly assess the quality of parts produced by SLM, it's critical to evaluate mechanical properties such as tensile strength and wear rate. These measurements provide insights into the material's durability, resistance to deformation under stress, and its performance under frictional forces, which are vital for numerous engineering applications. Below is an outline of how tensile strength and wear rate measurements were typically conducted in the current work.

Tensile test

Tensile test specimens are printed according to standard geometries specified in relevant standards (ASTM E8/E8M-15a) [63-64] through SLM process. Universal Testing Machine (UTM) is used for measuring tensile strength. The test specimen is mounted on the UTM using grips that align with the specimen's axis. The machine then pulls the specimen at a constant strain rate (0.2mm/sec), and data acquisition software records the force and displacement until the specimen fails.

Wear test

Wear test specimens are printed according to standard geometries specified in relevant standards (ASTM G99) thru SLM process and wear test was conducted by pin-on-disk method. The wear factors, such as load and sliding distance, are maintained at a constant value of 50N and 2000m, respectively, during the experiments. The sample is subjected to wear under specified conditions (load, speed, counter face material, and environment). The wear track is often measured periodically, and the test is conducted for a duration of 10 minutes. The wear rate was directly noted down from the computerized display unit from the experimental set up. These tests are essential for understanding the mechanical performance and durability of SLM-printed 17-4 PHSS parts. SEM studies were done for meticulously analyzing fracture and wear surface of the samples.

RESULTS AND DISCUSSION

The Taguchi L9 plan is employed for experiments and data collection, with subsequent statistical evaluation. Optimal parametric conditions are determined using Pareto ANOVA for various response functions. The super ranking method optimizes UTS and WR simultaneously. Validation experiments confirm model accuracy, with the detailed methodology presented in Fig. 5 for achieving high UTS and low wear rate.

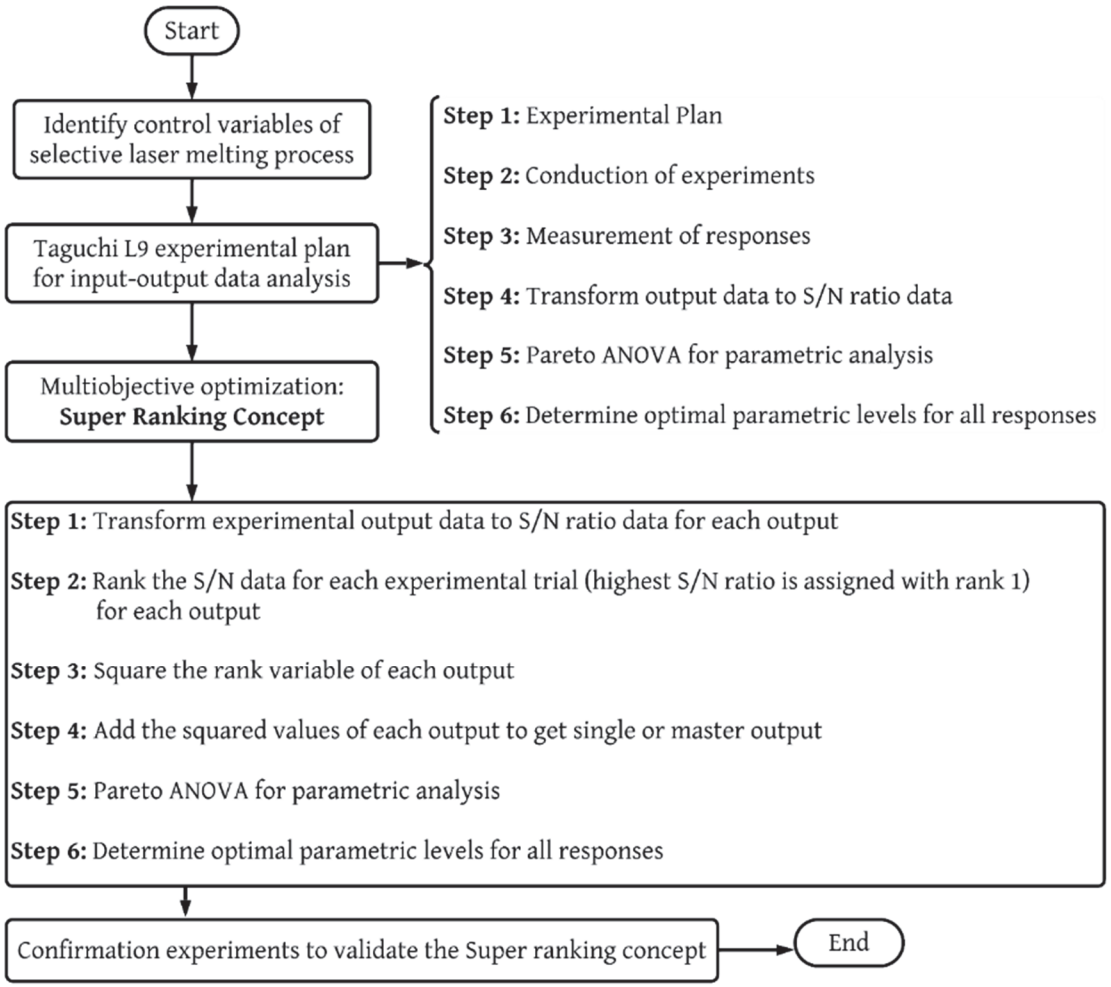

Figure 5: Framework in modelling and optimization of SLM Process.

DATA COLLECTION

SLM variables (LP, SS, and HD) influence the quality of build parts. Therefore, the L9 experimental plan was made for planning and experimentation, followed by data collection (refer to Table 2). Each trial run was repeated thrice and recorded the average values of three UTS and WR (refer to Table 2). The experimental output data is transformed to signal-to-noise ratio data-based quality characteristics with larger-the-better for UTS and smaller-the-better for WR (refer to Table 3). The S/N ratio output data is computed by applying equation 1 and 2. The computed values of the S/N ratio for each run are represented with i corresponding to *the* j^{th} output.

$$S/N_{UTS} = \eta_{ij} = -10\log\left(\frac{1}{n}\sum_{i=1}^{n}\frac{1}{\left(O_{ij}\right)^2}\right) \quad (1)$$

n = 1, 2,.....m; j = 1, 2,.....p

$$S/N_{WR} = \eta_{ij} = -10\log\left(\frac{1}{n}\sum_{i=1}^{n}\left(O_{ij}\right)^2\right) \quad (2)$$

Sl. No.	LP(W)	SS (mm/s)	HD (mm)	UTS (MPa)	WR (µm) at 50 N
1-SS	240	600	0.08	1112 ± **5.4**	92.86 ± 2.2
2-SS	240	800	0.10	1146 ± **4.8**	82.56 ± 1.4
3-SS	240	1000	0.12	1155 ± **6.3**	80.82 ± 3.7
4-SS	270	600	0.10	1173 ± **5.1**	80.59 ± 2.8
5-SS	270	800	0.12	1184 ± **3.2**	68.96 ± 4.3
6-SS	270	1000	0.08	1196 ± **4.1**	49.83 ± 3.5
7-SS	300	600	0.12	1185 ± **3.5**	65.60 ± 4.1
8-SS	300	800	0.08	1188 ± **2.6**	54.05 ± 2.7
9-SS	300	1000	0.10	1206 ± **1.7**	43.65 ± 3.6

Table 2: Input-output data of the SLM process.

Designation/ Exp. No.	S/N Ratio of UTS (dB)	S/N Ratio of wear rate (dB)
1-SS	60.92	-39.36
2-SS	61.18	-38.34
3-SS	61.25	-38.15
4-SS	61.39	-38.13
5-SS	61.47	-36.77
6-SS	61.55	-33.95
7-SS	61.47	-36.34
8-SS	61.50	-34.66
9-SS	61.63	-32.80

Table 3: S/N ratio results of UTS and WR of 17-4PH Stainless Steel Sample.

PARETO ANOVA

To obtain better performance in SLM build parts, appropriate control of process variables and their behavioral insights on quality characteristics (i.e., outputs) are of industrial relevance. Pareto analysis of the variance table is constructed wherein the individual factor significance on the output is estimated. The factor's significance on outputs could help the industry personnel provide detailed process insights. S/N ratio with higher-the-better quality characteristics data were used to construct the Pareto ANOVA table. Pareto ANOVA tables comprise sum at factor levels (SFL), the sum of squares of differences (SSD), percent contribution and optimal parametric condition. The sample computation of SFL, SSD, and PC is presented in Table 4. Notably, higher values of the S/N ratio are treated as best once the actual output is transformed into S/N ratio data, irrespective of lower-the-better or higher-the-better quality characteristics. SFL is estimated to determine the factor effects (i.e., parametric significance) and percent contribution on individual output. SSD is an essential parameter to determine the percent contribution of individual factors to the output analyzed. The significance of parametric contribution is estimated for the preset confidence level set at 95%. The highest

PC value is designated as the dominant factor influencing output. The PC value of less than 5% signifies that the factor is insignificant. The optimal parametric conditions of SLM process variables are determined corresponding to the highest value of SFL for each factor.

Pareto Anova for UTS

The individual factor effects of SLM variables were analyzed (subjected to three operating levels: low, medium, and high) on the performance of UTS are presented in Fig 6. Low and medium values of LP (240 W and 270 W) resulted in lower UTS values. Low LP value causes lesser energy density (energy density is directly proportionate to LP, wherein lower LP results in lesser energy density), resulting in unmelt metal powders when building the parts. The unmelt powder causes pores, voids, or discontinuities around the coarse-grained solidified structure, resulting in premature failure in-built parts [65]. The lesser energy density ensures that a small quantity of molten metal remains liquid for a short duration, resulting in microporosity in SLM-built parts [66]. A higher laser power of 300 W is sufficient to melt all metal powders to produce strong parts with minimal defects, resulting in better tensile strength in the SLM parts. Increased values of SS from 600-1000 mm/s showed higher UTS (refer to Fig. 6).

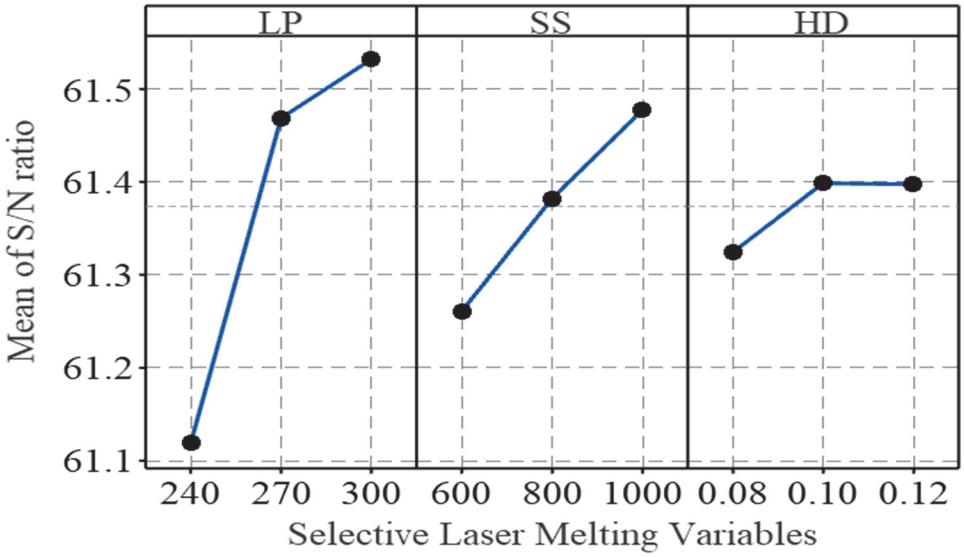

Figure 6: Main factor effects for ultimate tensile strength (S/N ratio).

Lower UTS values recorded with scan speed maintained at 600 mm/s are attributed to the following reasons [67-68]: lower SS require higher temperature to melt all metal powders and low melting temperature due to lower SS causes many metal powders to remain un-melt in dense powdered particles leading to void or pore formation in-built parts. Higher SS ensure better fusion characteristics, ensuring all metal powders undergo melt and fill the pores (present, if any) tends to produce sound strength inbuilt part [69-Xie et al. 2021]. Hatch distance increased from 0.08-0.1 mm, resulting in improved UTS, and after that (i.e., up to 0.12 mm) showed negligible change in UTS. The overlap between the melt track decreases with a proportionate increase in HD. Lower HD tends to melt the already solidified layer on the build parts, causing vaporizing or burning of metal with defects remaining on the metal parts, causing lower UTS. The PC contribution of LP, SS and HD on UTS was 78.42%, 18.7% and 2.88%, respectively. HD was found to have a negligible effect due to their lower PC and was consistent with published literature [70-Sheshadri et al. 2021]. The optimal parametric conditions determined viz. Pareto ANOVA is $LP_3SS_3HD_2$ (LP: 300 W, SS: 1000 mm/s, and HD: 0.1 mm). The determined optimal conditions are from the L9 orthogonal array experiments (Experiment No. 9 or 9-SS).

Pareto ANOVA for WR

Fig. 7 presents the details of the main effect plots drawn from the S/N ratio values of WR. An increase in LP from 240 to 300 W resulted in higher wear resistance in SLM parts. Lower LP may not be sufficient to raise the temperature required enough to melt all metal powders, causing pores and discontinuities around the unmelt metal powders. Higher wear rates at lower LP in the SLM build parts are attributed to unmelted metal particles inside the pores [71]. SLM parts were built by the powdered layer possessing predefined thickness by the CAD model. The SS varied during experimentation, ranging from 600-1000 mm/s, resulting in a linear increase in wear resistance (i.e., decreased WR). The material undergoes a rapid

temperature rise, resulting in a dense liquid pool and even the possibility of re-melt the already solidified layers, ensuring the fill of pores (present, if any) at higher SS [71]. The effect of hatch distance on wear rate is presented in Fig. 7. The HD determines the overlap size of scan tracks. Lower HD ensures more overlaps on the build parts, resulting in higher energy density input, which causes a more stable liquid pool to fuse the metal powders [72]. Note that the melt pool becomes unstable and inadequate melting due to reduced heat input with increased HD beyond the critical value [73]. The above phenomenon results in better compact density and, therefore, lesser WR. The mathematical computation could help to determine the effects of an individual factor in terms of percent contribution for LP, SS, and HD equal to 61.72%, 33.63% and 4.65%, respectively. Pareto ANOVA determined optimal condition for low wear rate in SLM parts is LP3SS3HD1 (LP: 300 W, SS: 1000 mm/s, and HD: 0.08 mm. The optimal conditions are found different to that of L9 experiments (refer to Table 2) and are expected probably due to multi-factor nature of total nine experiments performed compared to that of 27 (Number Levels $^{factors} = 3^3$) [74-76]. The practical utility of the model determined optimal conditions were confirmed by conducting practical experiments resulting in a reduced wear rate of 41.23 ± 1.7 μm.

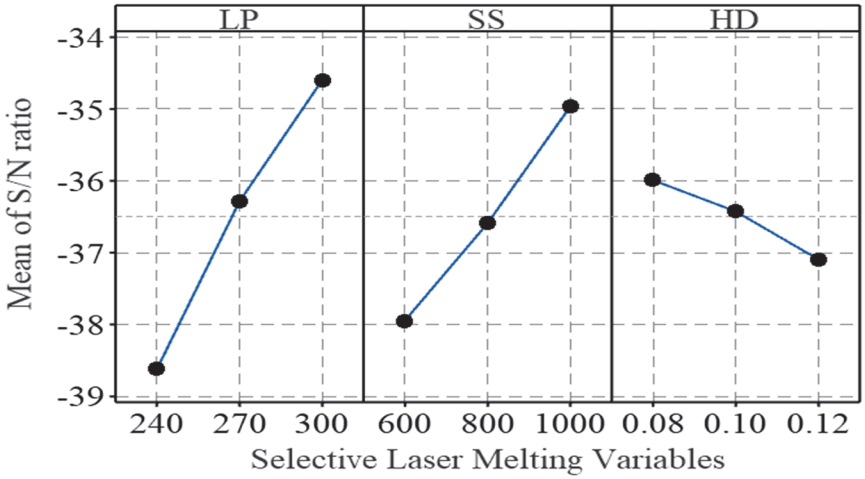

Figure 7: Main factor effects for wear rate (S/N ratio).

Responses		Ultimate tensile strength				Wear rate			
Factor	Level	LP	SS	HD	Total	LP	SS	HD	Total
Sum at factor levels	1	183.36*	183.78	183.97	552.4	-115.84	-113.82	-107.96	-328.5
	2	184.41	184.15	184.20		-108.85	-109.76	-109.26	
	3	184.60	184.43	184.19		-103.79	-104.90	-111.26	
The sum of squares of differences		2.68**	0.64	0.10	3.41	219.64	119.69	16.56	355.9
Per cent contribution		78.42***	18.70	2.88	100	61.72	33.63	4.65	100
Optimal levels		$LP_3SS_3HD_2$				$LP_3SS_3HD_1$			
$183.36^* = 60.92 + 61.18 + 61.25$ $2.68^{**} = ((183.36 - 184.41)^2 + (183.36 - 184.60)^2 + (183.41 - 184.6)^2)$ $78.42^{***} = 100*(2.68/3.41)$									

Table 4: Pareto ANOVA (based on S/N ratio) results for UTS and WR

Multiple objective optimizations: Super Ranking Concept

Taguchi determined the optimal conditions for maximizing the UTS LP3SS3HD2 and minimizing the WR $LP_3SS_3HD_1$. The single optimal condition can only be determined subjected to multiple objective optimizations, i.e., SRC. Multiple objective optimizations determine many potential solutions and rely on assigned weight fractions to individual objective functions.

SRC estimate a single optimal condition for multiple outputs without assigning the weight fractions. The mathematical steps illustrating determining the optimal solutions for multiple outputs corresponding to a single parametric condition are presented in Fig. 5. The individual factor effects on combined responses (SSR: WR + UTS) were estimated by constructing the Pareto ANOVA. Note that the Pareto ANOVA table was constructed based on the actual values of SSR. LP was found to have a dominant effect with the highest contribution equal to 81.01%, followed by SS and HD, equal to 18.66% and 0.33%, respectively. Note that the minimum values of SSR (the sum of all the squared rankings) are considered the optimal condition. Rank 1 corresponds to the highest S/N ratio values among the L9 experimental trials. Therefore, minimum values corresponding to the sum at each factor level were treated as optimal conditions for the SLM process. SLM's optimal parametric condition that satisfies both WR and UTS is LP3SS3HD3 (LP: 300 W, SS: 1000 mm/s, and HD: 0.12 mm). Interestingly, the SRC determined optimal conditions are not from L9 experiments (refer to Table 2) and therefore, confirmatory experiments were carried out to validate model accuracy. The determined optimal conditions resulted experimentally the WR and UTS equal to 47.65 ± 1.9 μm and 1197 ± 5.3 MPa.

Sl. No.	Input Variables			Ranking		Squared Ranking		SSR
	LP, W	SS, mm/s	HD, mm	UTS	WR	UTS	WR	
1-SS	240	600	0.08	9	9	81	81	162
2-SS	240	800	0.10	8	8	64	64	128
3-SS	240	1000	0.12	7	7	49	49	98
4-SS	270	600	0.10	6	6	36	36	72
5-SS	270	800	0.12	4	5	16	25	41
6-SS	270	1000	0.08	2	2	4	4	8
7-SS	300	600	0.12	5	4	25	16	41
8-SS	300	800	0.08	3	3	9	9	18
9-SS	300	1000	0.10	1	1	1	1	2

Table 5: Super ranking concept-based multiobjective optimization of SLM process (*SSR: sum of squared ranking).

Factors	Levels	LP	SS	HD	Total
Sum at factor levels	1	388	275	188	453.7
	2	121	187	202	
	3	61	108	180	
A sum of squares of differences		181818	41874	744	9.74
Per cent contribution		81.01	18.66	0.33	100
Optimal levels	$LP_3SS_3HD_3$				

Table 6: Pareto ANOVA results for Super Ranking Concept.

Fracture surface analysis

Fig. 8 depicts tensile fracture surface morphology of 17-4 PHSS samples at different conditions. From the fracture surfaces different features such as curved voids, gas porosity, keyhole void, rapid fracture facet, dimples and stream flow patterns are observed.

Fig. 8(a) depicts fractographs of 17-4 PHSS at LP1SS1HD1 condition (LP: 240 W, SS: 600 mm/s, and HD: 0.08 mm) displaying ductile-brittle fracture due to the presence of rapid fracture facet, uneven small sized dimples (~1 to 2 μm) was detected throughout the surface with flat surface at few regions, these surfaces influenced a even rupture surface owing to rapid fracture and parting of two contiguous grains. The presence of both rapid fracture facets and dimples indicates that the material experienced a combination of ductile and brittle fracture mechanisms. The rapid fracture facets are indicative of brittle failure, where crack propagation occurs rapidly without significant plastic deformation. In contrast, the dimples suggest areas of ductile failure, where the material underwent some degree of plastic deformation before failure. AM specimen failure was also attributed due to surface severity brought on by internal voids formed by unmelted particles and gas entrapment. Similar observations were made by Aripin et al. [77].

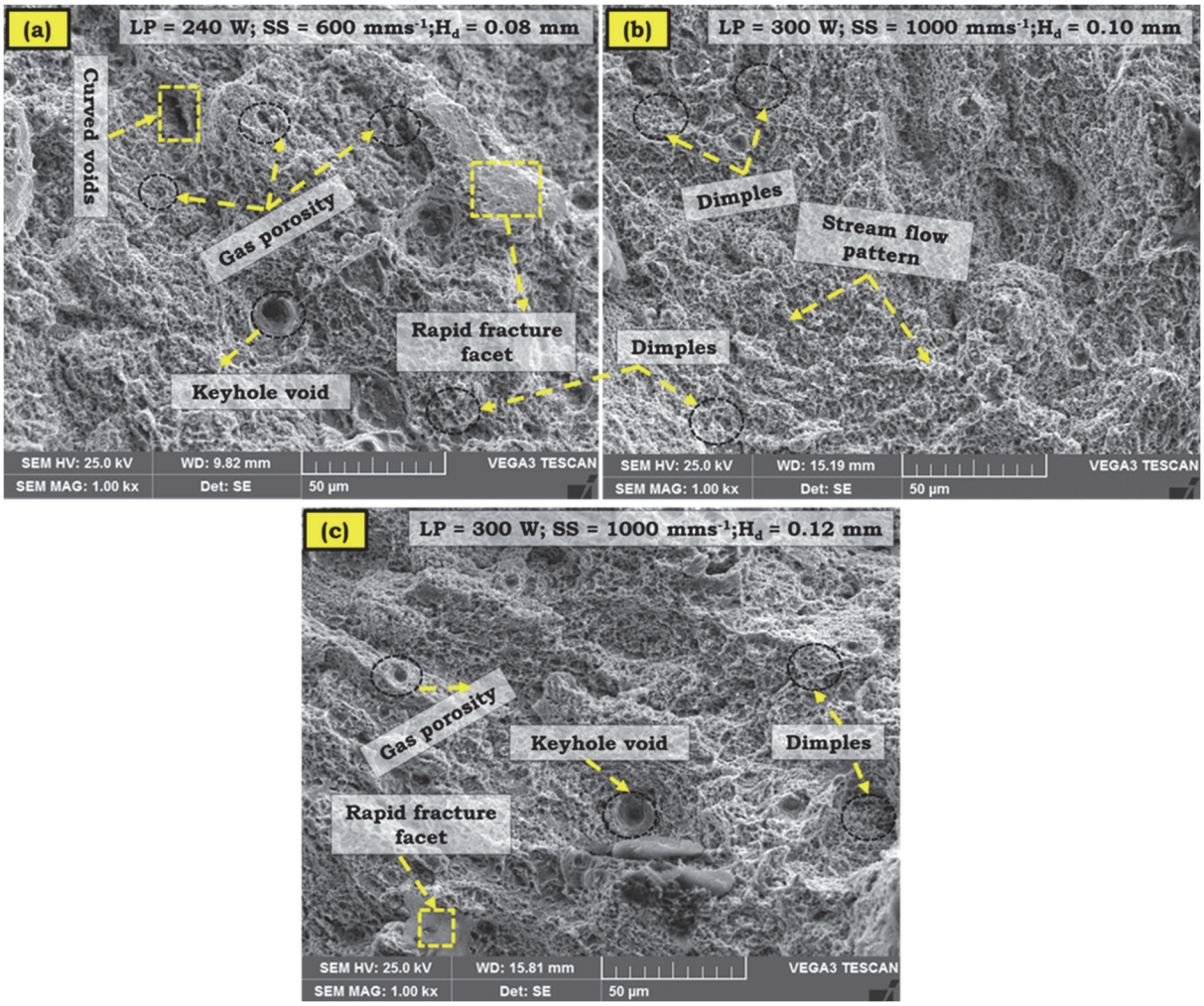

Figure 8: Tensile fracture surface morphology of (a) 17-4 PHSS sample at LP1SS1HD1 condition (b) 17-4 PHSS sample at LP3SS3HD2 condition (c) 17-4 PHSS sample at LP3SS3HD3 condition.

Fig. 8(b) depicts fractographs of 17-4 PHSS at LP3SS3HD2 condition (LP: 300 W, SS: 1000 mm/s, and HD: 0.10 mm) displaying ductile fracture due to the presence of fine sized dimples throughout the region with river flow patterns. The presence of fine-sized dimples across the fracture surface is a classic indicator of ductile fracture, where the material undergoes significant plastic deformation prior to failure. Dimples form through the nucleation, growth, and coalescence of micro voids under tensile stress. The fine size of these dimples suggests a relatively uniform and controlled deformation process, likely facilitated by the optimized energy input and material interaction under the LP3SS3HD2 condition. The observation of river flow patterns alongside dimples further supports the ductile nature of the fracture. River flow patterns are indicative of localized plastic deformation and are typically observed in materials that have undergone significant ductile tearing. These patterns can also highlight the direction of crack propagation through the material, providing insights into the stress state during failure. These results are in line with Aripin et al.'s microstructure findings [77]. Also, less voids, curled voids, gas porosity, keyhole void are observed in Fig. 8(b).

Fig. 8(c) depicts fractographs of 17-4 PHSS at LP3SS3HD3 condition (LP: 300 W, SS: 1000 mm/s, and HD: 0.12 mm) displaying ductile fracture due to the presence of fine sized dimples throughout the region with voids and gas porosity at few places. The uniform distribution and equivalent size of the dimples on the fracture surface could result in a significant extent of extension. Also, the presence of fine-sized dimples across the entire fracture surface is a hallmark of ductile fracture. Dimples are micro voids that form as the material undergoes plastic deformation, indicating that the material absorbed a significant amount of energy before failing. The uniform distribution and equivalent size of the dimples suggest a consistent and homogeneous material response to stress across the fracture surface, likely leading to enhanced ductility and fracture toughness. A common ductile fracture mechanism called necking phenomena was clearly seen on the sample's

fracture surface. additionally producing holes and cleavage surfaces in a few areas of the sample. These results are in line with Zhao et al.'s microstructure findings [78].
Overall, it can be observed that LP3SS3HD3 condition has generally promoted ductile fracture characteristics in 17-4 PHSS, indicative of good material toughness and deformability, attention must be paid to minimizing defects like voids and gas porosity to further improve material performance.

Wear surface analysis

Fig. 9 depicts SEM morphology of 17-4 PHSS samples. The SEM microstructure of the 17-4 PHSS sample, as obtained, is shown in Fig. 9(a). It shows a finely defined, characteristic columnlike plank-form martensitic structure within identifiable preceding austenite grains. Also, at this resolution (2.00kx) elongated structure made up of a few different shades ranging from darkish to bright is observed along porosity at few areas. According to Ponnusamy et al., martensite was seen as a darkish, popping area with undefined regions [79].
From Figs. 9(b), (c) and (d), numbering 1 to 7 denotes sliding direction, abrasive worn-out area, specks, deep abrasive pits, thick grooves, thin grooves, and narrow abrasive pits.
Fig. 9(b) depicts wear track of 17-4 PHSS at LP1SS1HD1 condition (LP: 240 W, SS: 600 mm/s, and HD: 0.08 mm) displaying extensive wear-out surface characterized by abrasive worn-out area, specks, deep abrasive pits, thick grooves throughout the surface. The wear track also indicates that the material surface has undergone significant degradation due to abrasive wear, indicated by aforesaid characteristics (specks, deep abrasive pits, thick grooves) indicating that the material has been deformed due to hard protuberances forced against and moving along the surface.

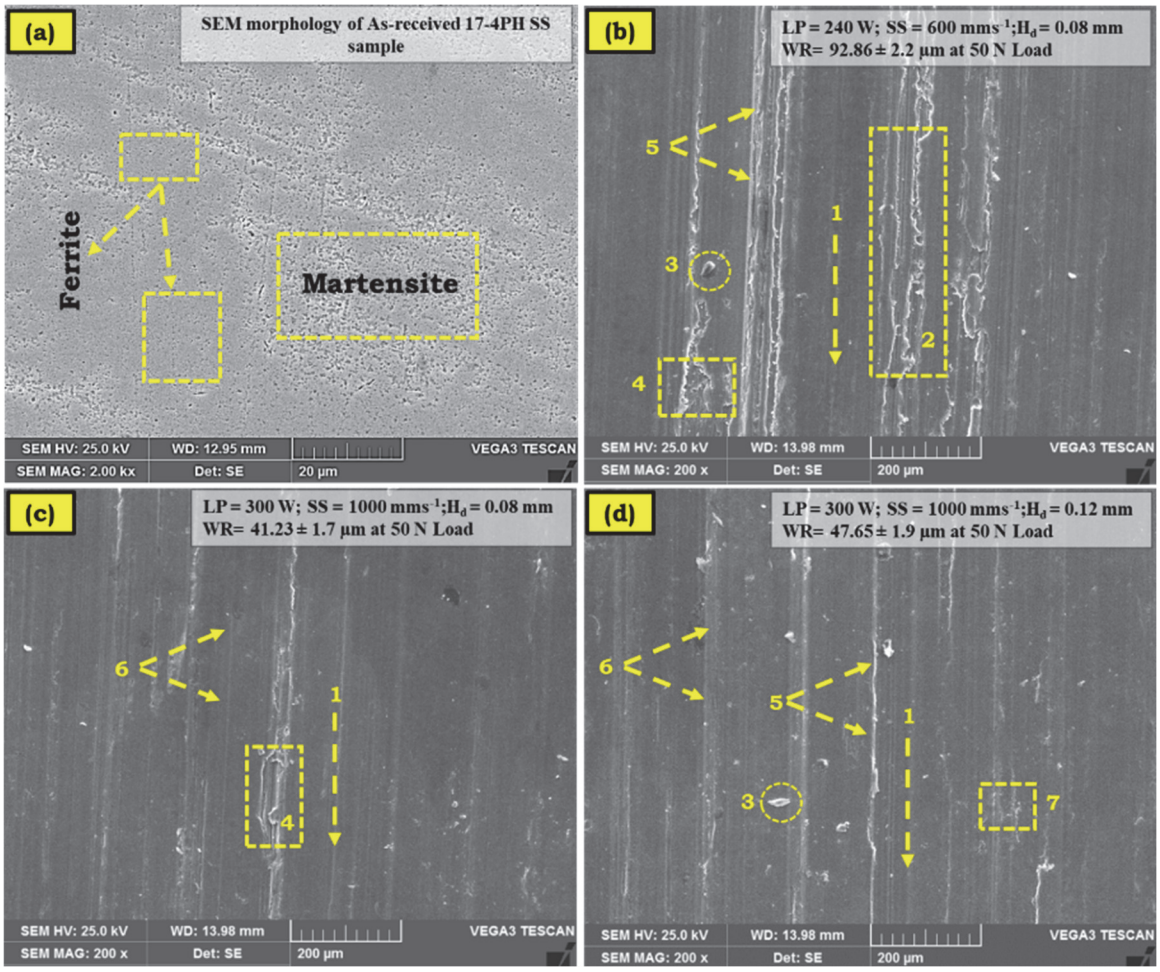

Figure 9: SEM morphology of (a) As-received 17-4 PHSS sample (b) Extensive worn-out surface (c) Least worn-out surface (d) Moderate worn-out surface.

Fig. 9(c) depicts wear track of 17-4 PHSS at LP3SS3HD1 condition (LP: 300 W, SS: 1000 mm/s, and HD: 0.08 mm) displaying least wear-out surface characterized by abrasive pits at few areas followed by thin grooves throughout the surface.

The wear features also indicated that abrasive pits and thin grooves across few areas reduced intensity of wear compared to the extensive wear-out surface observed under the LP1SS1HD1 condition. The presence of abrasive pits indicates that there are still interactions between the surface and hard particles, but these interactions are less severe or less frequent. Similarly, the existence of thin grooves rather than thick ones suggests a lighter or less aggressive wear mechanism at play. Fig. 9(d) depicts wear track of 17-4 PHSS at LP3SS3HD3 condition (LP: 300 W, SS: 1000 mm/s, and HD: 0.12 mm) displaying moderate wear-out surface characterized by narrow pits followed by thick and thin grooves at few areas in the worn-out surface. The wear features also indicated that a moderate wear-out surface, which suggests a wear severity that lies between the extensive wear observed in the LP1SS1HD1 condition and the minimal wear found under LP3SS3HD1 conditions. The presence of narrow pits, along with both thick and thin grooves, indicates a variety of wear mechanisms at play. The narrow pits could suggest localized points of high stress or material removal, possibly due to the impact of hard particles or asperities on the surface. The variation in groove thickness may reflect differences in the forces or movements experienced by different parts of the surface during wear, with thick grooves indicating areas of higher stress or more aggressive wear, and thin grooves pointing to areas where the wear was less severe. Overall, it can be observed that The variation in wear patterns, seen by comparing the conditions LP1SS1HD1, LP3SS3HD1, and LP3SS3HD3, underscores the complexity of wear mechanisms and the significant influence of manufacturing parameters on material wear characteristics. Specifically, the increase in hatch distance from 0.08 mm in LP3SS3HD1 to 0.12 mm in LP3SS3HD3, while keeping the laser power and scan speed constant, suggests that even small changes in processing parameters can have noticeable effects on the wear resistance of of 17-4 PHSS samples at different conditions. [70,80].

EDAX analysis of fracture and wear surface

Fig. 10(a) and (b) display the EDAX analysis of fracture surface and wear surface of 17-4 PHSS sample at LP3SS3HD3 condition respectively. From the EDAX analysis it's clear that 17-4 PHSS mainly consists of Fe, followed by Cr, Ni and Cu followed by traces of other elements.

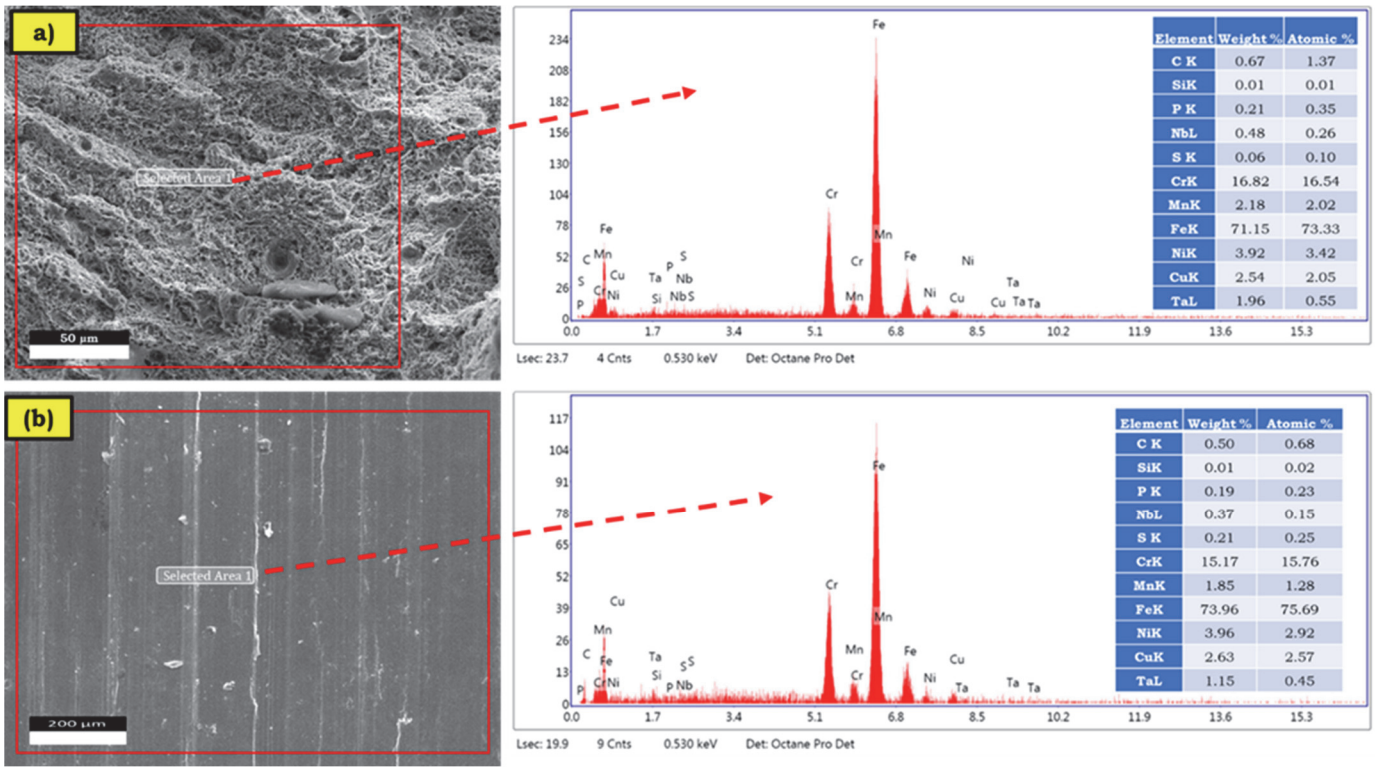

Figure 10: (a) and (b) show EDAX analysis of fracture and wear surfaces of 17-4 PHSS samples. Analysis reveals Fe as the main element, with Cr, Ni, Cu, and traces of other elements present.

Microstructure analysis

The final characteristics of a component are determined by its microstructural attributes. This study investigated the morphology of 17-4PH stainless steel (SS) using optical (OM) and scanning electron microscopy (SEM). Figs. 11(a), (b), (c),

and (d) display micrographs of as-built SLM 17-4PH SS samples. These figures illustrate different printing parameters: LP1SS1HD1 (LP: 240 W, SS: 600 mm/s, and HD: 0.08 mm) and LP3SS3HD2 (LP: 300 W, SS: 1000 mm/s, and HD: 0.10 mm). The samples were produced via SLM in an upright path.

The microstructural analysis shows a combination of two phases, martensite and austenite, with distinct variations seen between the two groups of samples. Figs. 10(a)and(b) displays the as-built OM and SEM microstructures of the 17-4PH SS sample. Fig. 11(b) displays striation-shaped cross-sections of the melt pools, which are identifiable as being parallel to the direction of construction. The laser scans create melt pool characteristics that exhibit irregularly shaped holes and voids. These accumulate near the margins of the melt pools, most likely as a result of gas being trapped. The presence of gaps and voids can be partially ascribed to the utilisation of preset procedure settings, that can result in localised process disruptions and inefficiencies linked to subpar mechanical and wear characteristics. The presence of porosity in the material can have an immense impact on its mechanical properties, since it may serve as places where cracks can start.

Figs. 11(c) and 10(d) show a distinct, well-defined pilaster-like plank-form martensitic structure inside identifiable austenite grains. Figs. 10(c) and 10(d) exhibit a reduced number of pores and voids in comparison to Figs. 11(a) and 11(b), resulting in enhanced mechanical and wear characteristics.

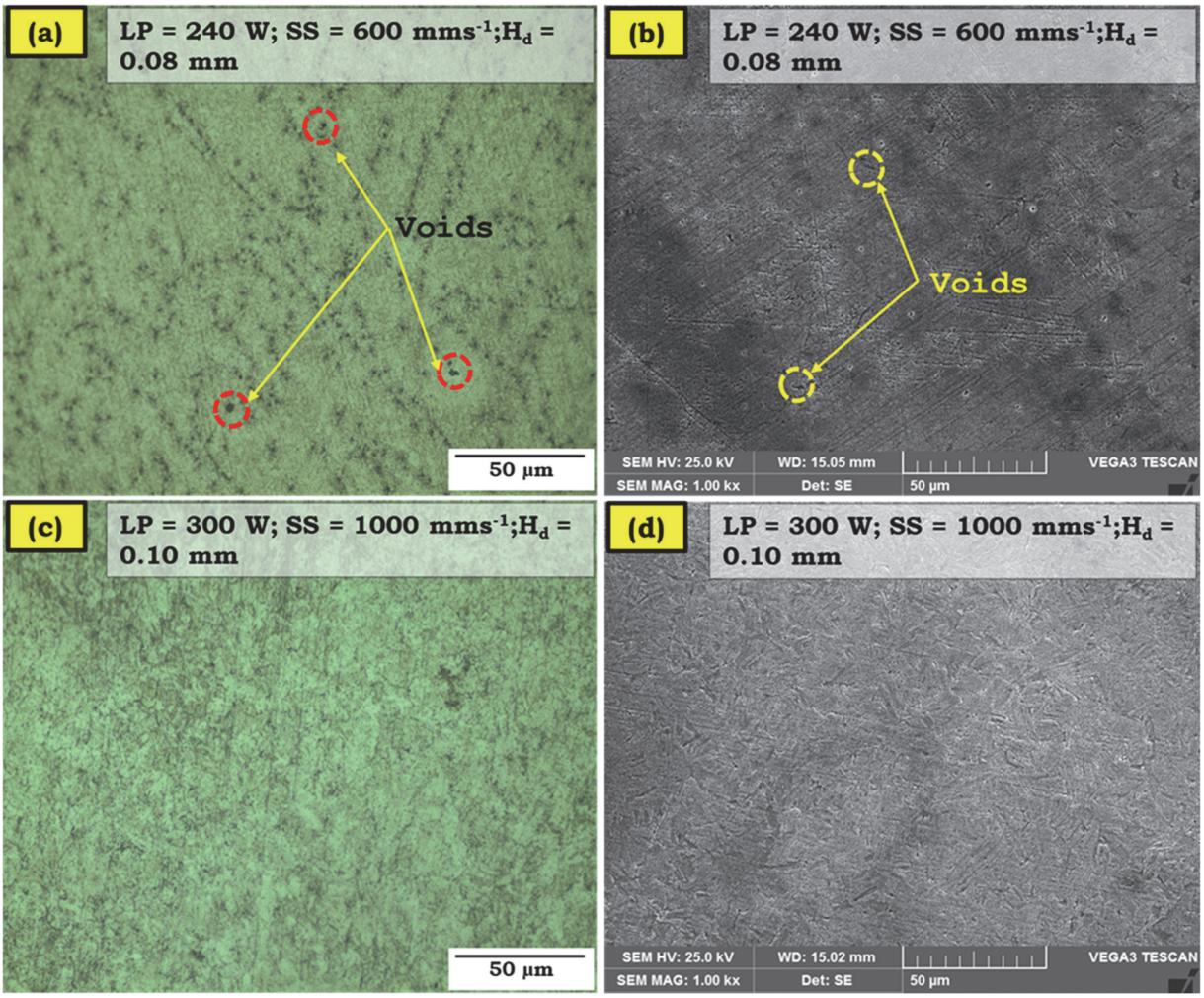

Figure 11: Micrographs of (a) and (b) Optical and Scanning electron micrographs of as-received 17-4 PHSS sample at LP1SS1HD1 condition. (c) and (d) Optical and Scanning electron micrographs of as-received 17-4 PHSS sample at LP3SS3HD2 condition

Conclusion

The SLM process route is applied to print the 17-4 PH SS according to Taguchi L9 experimental plan. Printed parts' ultimate tensile strength and wear rate were analyzed statistically to determine the parametric influence and optimize individually and simultaneously. The following conclusions were drawn:

1. EDAX analysis confirms the composition (Fe: 71.7%, Cr: 18.44%, Ni: 3.86%, Cu: 3.51%) of 17-4 PH SS in printed parts. The powdered particles exhibited annular morphology and displayed an average size of 30 ± 5 μm.
2. LP of 300 W melted all metal powders to produce parts with minimal or no defects, resulting in better tensile strength in the SLM parts. A higher SS of 1000 mm/s ensure better fusion characteristics, ensuring all metal powders melt and fill pores (present, if any) to produce better strength in-built parts. Lower and higher HD showed adverse effects on UTS. The LP, SS and HD contributions on UTS were 78.42%, 18.7% and 2.88%. The LP: 300 W, SS: 1000 mm/s, and HD: 0.1 mm produced the highest UTS equal to 1206 MPa.
3. Higher WR was recorded at a lower LP of 240W, attributed to the unmelted metal particles inside the pores. A higher SS of 1000 mm/s raise the metal temperature to cause a dense molten pool and has a greater probability of remelting the already solidified layers to fill pores present, if any, in part. The melt pool becomes unstable due to inadequate melting due to reduced heat input with increased HD beyond the critical value of 0.08 mm, resulting in higher WR. The optimal condition for a low wear rate of 41.23 ± 1.7 μm is achieved in SLM parts for the process variable set at LP: 300 W, SS: 1000 mm/s, and HD: 0.08 mm.
4. The super-ranking concept determined the optimal condition for multiple outputs (UTS and WR). LP was found to have a dominant effect with the highest contribution, equal to 81.01%, followed by SS and HD, equal to 18.66% and 0.33%. SRC determined optimal conditions (LP: 300 W, SS: 1000 mm/s, and HD: 0.12 mm), resulting experimentally in the WR and UTS equal to 47.65 ± 1.9 μm and 1197 ± 5.3 MPa.
5. The fracture surface morphology of 17-4 PHSS samples at different conditions indicated different failures. 17-4 PHSS samples LP1SS1HD1 condition (LP: 240 W, SS: 600 mm/s, and HD: 0.08 mm) displaying ductile-brittle fracture followed by LP3SS3HD2 and LP3SS3HD3 conditions displaying ductile failure.
6. The variation in wear patterns, seen by comparing the conditions LP1SS1HD1, LP3SS3HD1, and LP3SS3HD3, underscores the complexity of wear mechanisms and the significant influence of manufacturing parameters on material wear characteristics. Specifically, the increase in hatch distance from 0.08 mm in LP3SS3HD1 to 0.12 mm in LP3SS3HD3, keeping the laser power and scan speed constant, suggests that even small changes in processing parameters can have noticeable effects on the wear resistance of 17-4 PHSS samples at different conditions.

REFERENCES

[1] Garrison, W.M. (1990). Ultrahigh-strength steels for aerospace applications, JOM, 42, pp. 20-24. DOI: 10.1007/BF03220942.

[2] De Nisi, J., Pozzi, F., Folgarait, P., Ceselin, G. and Ronci, M. (2019). Precipitation hardening stainless steel produced by powder bed fusion: Influence of positioning and heat treatment, Procedia Struct. Integr., 24, pp. 541-558. DOI: 10.1016/j.prostr.2020.02.048.

[3] Ravitej, S.V., Murthy, M. and Krishnappa, M. (2018). Review paper on optimization of process parameters in turning Custom 465® precipitation hardened stainless steel, Mater. Today: Proc., 5(1), pp. 2787-2794. DOI: 10.1016/j.matpr.2018.01.066.

[4] Mróz, M., Kucel, B., Rąb, P. and Olszewska, S. (2023). Study of the TIG Welding Process of Thin-Walled Components Made of 17-4 PH Steel in the Aspect of Weld Distortion Distribution, Materials, 16(13), pp. 4854. DOI: 10.3390/ma16134854.

[5] Gholipour, A., Shamanian, M. and Ashrafizadeh, F. (2011). Microstructure and wear behavior of stellite cladding on 17-4 PH stainless steel, J. Alloys Compd., 509(14), pp. 4905-4909. DOI: 10.1016/j.jallcom.2010.09.216.

[6] Bressan, J.D., Daros, D.P., Sokolowski, A., Mesquita, R.A. and Barbosa, C.A. (2008). Influence of hardness on the wear resistance of 17-4 PH stainless steel evaluated by the pin-on-disc testing, J. Mater. Process. Technol., 205(1-3), pp. 353-359. DOI: 10.1016/j.jmatprotec.2007.11.251.

[7] Ghaffari, M., Nemani, A.V. and Nasiri, A. (2022). Microstructure and mechanical behavior of PH 13–8Mo martensitic stainless steel fabricated by wire arc additive manufacturing, Addit. Manuf., 49, pp. 102374. DOI: 10.1016/j.addma.2021.102374.

[8] Zai, L., Zhang, C., Wang, Y., Guo, W., Wellmann, D., Tong, X. and Tian, Y. (2020). Laser powder bed fusion of precipitation-hardened martensitic stainless steels: a review, Metals, 10(2), pp. 255. DOI: 10.3390/met10020255.

[9] Sarkar, S., Kumar, C.S. and Nath, A.K. (2017). Effect of mean stresses on mode of failures and fatigue life of selective laser melted stainless steel, Mater. Sci. Eng. A, 700, pp. 92-106. DOI: 10.1016/j.msea.2017.05.118.

[10] Arisoy, C.F., Başman, G. and Şeşen, M.K. (2003). Failure of a 17-4 PH stainless steel sailboat propeller shaft. Eng. Fail. Anal., 10(6), pp. 711-717. DOI: 10.1016/S1350-6307(03)00041-4.
[11] Grujicic, M., Yavari, R., Snipes, J.S., Ramaswami, S., Yen, C.F. and Cheeseman, B.A. (2014). Linear friction welding process model for carpenter custom 465 precipitation-hardened martensitic stainless steel, J. Mater. Eng. Perform., 23, pp. 2182-2198. DOI: 10.1007/s11665-014-0985-9.
[12] Mohanty, O.N. (2017). Forging Grade Steels for Automotives, In Automotive Steels (pp. 413-453). Woodhead Publishing. DOI: 10.1016/B978-0-08-100638-2.00013-4.
[13] Sivaiah, P. and Chakradhar, D. (2019). Modeling and optimization of sustainable manufacturing process in machining of 17-4 PH stainless steel, Measurement, 134, pp. 142-152. DOI: 10.1016/j.measurement.2018.10.067.
[14] Zhang, X. and Liou, F. (2021). Introduction to additive manufacturing, Additive manufacturing, pp. 1-31. DOI: 10.1016/B978-0-12-818411-0.00009-4.
[15] Liu, Y., Zhang, Z., Li, G., Wang, Q., Wang, L. and Li, B. (2017). Effect of current on structure and macrosegregation in dual alloy ingot processed by electroslag remelting, Metals, 7(6), pp. 185. DOI: 10.3390/met7060185.
[16] Mahmoodi, H., Abbasi, M. and Hosseinipour, S.J. (2023). The effect of renewed melting process under electrical slag on the fatigue life of the precipitation hardened stainless steel Custom-450, J. Mater. Res. Technol., 23, pp. 1680-1695. DOI: 10.1016/j.jmrt.2023.01.070.
[17] Durakovic, B. (2018). Design for additive manufacturing: Benefits, trends and challenges. Period. Eng. Nat. Sci., 6(2), pp. 179-191. DOI: 10.21533/pen.
[18] Atzeni, E. and Salmi, A. (2012). Economics of additive manufacturing for end-usable metal parts, Int. J. Adv. Manuf. Technol., 62, pp. 1147-1155. DOI: 10.1007/s00170-011-3878-1.
[19] Caputo, M.P., Berkowitz, A.E., Armstrong, A., Müllner, P. and Solomon, C.V. (2018). 4D printing of net shape parts made from Ni-Mn-Ga magnetic shape-memory alloys, Addit. Manuf., 21, pp. 579-588. DOI: 10.1016/j.addma.2018.03.028.
[20] Walter, A. and Marcham, C.L. (2020). Environmental advantages in additive manufacturing, Prof. Saf., 65(01), pp. 34-38. Retrieved from https://commons.erau.edu/publication/1365.
[21] Javaid, M., Haleem, A., Singh, R.P., Suman, R. and Rab, S. (2021). Role of additive manufacturing applications towards environmental sustainability, Adv. Ind. Eng. Polym., 4(4), pp. 312-322. DOI: 10.1016/j.aiepr.2021.07.005.
[22] Kadkhoda-Ahmadi, S., Hassan, A. and Asadollahi-Yazdi, E. (2019). Process and resource selection methodology in design for additive manufacturing, Int. J. Adv. Manuf. Technol., 104, pp. 2013-2029. DOI: 10.1007/s00170-019-03991-w.
[23] Gibson, I., Rosen, D., Stucker, B. and Khorasani, M. (2014). Additive Manufacturing Technologies, 17, Springer. DOI: 10.1007/978-3-030-56127-7.
[24] Liu, W., Zhu, Z. and Ye, S. (2020). A decision-making methodology integrated in product design for additive manufacturing process selection, Rapid Prototyp. J., 26(5), pp. 895-909. DOI: 10.1108/RPJ-06-2019-0174.
[25] Zhang, D., Sun, S., Qiu, D., Gibson, M.A., Dargusch, M.S., Brandt, M., Qian, M. and Easton, M. (2018). Metal alloys for fusion-based additive manufacturing, Adv. Eng. Mater., 20(5), pp. 1700952. DOI: 10.1002/adem.201700952.
[26] Ardila, L.C., Garciandia, F., González-Díaz, J.B., Álvarez, P., Echeverria, A., Petite, M.M., Deffley, R. and Ochoa, J. (2014). Effect of IN718 recycled powder reuse on properties of parts manufactured by means of selective laser melting, Phys. Procedia, 56, pp. 99-107. DOI: 10.1016/j.phpro.2014.08.152.
[27] Gisario, A., Kazarian, M., Martina, F. and Mehrpouya, M. (2019). Metal additive manufacturing in the commercial aviation industry: A review, J. Manuf. Syst., 53, pp. 124-149. DOI: 10.1016/j.jmsy.2019.08.005.
[28] Yu, W., Sing, S.L., Chua, C.K. and Tian, X. (2019). Influence of re-melting on surface roughness and porosity of AlSi10Mg parts fabricated by selective laser melting, J. Alloys Compd., 792, pp. 574-581. DOI: 10.1016/j.jallcom.2019.04.017.
[29] Karimi, J., Suryanarayana, C., Okulov, I. and Prashanth, K.G. (2021). Selective laser melting of Ti6Al4V: Effect of laser re-melting, Mater. Sci. Eng. A, 805, pp. 140558. DOI: 10.1016/j.msea.2020.140558.
[30] Yasa, E., Deckers, J. and Kruth, J.P. (2011). The investigation of the influence of laser re-melting on density, surface quality and microstructure of selective laser melting parts, Rapid Prototyp. J., 17(5), pp. 312-327. DOI: 10.1108/13552541111156450.
[31] Boschetto, A., Bottini, L. and Pilone, D. (2021). Effect of laser remelting on surface roughness and microstructure of AlSi10Mg selective laser melting manufactured parts. Int. J. Adv. Manuf. Technol., 113, pp. 2739-2759. DOI: 10.1007/s00170-021-06775-3.
[32] Xiong, Z., Zhang, P., Tan, C., Dong, D., Ma, W. and Yu, K. (2020). Selective laser melting and remelting of pure tungsten, Adv. Eng. Mater., 22(3), pp. 1901352. DOI: 10.1002/adem.201901352.

[33] Khan, H.M., Özer, G., Tarakci, G., Coskun, M., Koc, E. and Kaynak, Y.U.S.U.F. (2021). The impact of aging and drag-finishing on the surface integrity and corrosion behavior of the selective laser melted maraging steel samples, Mater. Werkst., 52(1), 60-73.
[34] Wang, G., Liu, Q., Rao, H., Liu, H. and Qiu, C. (2020). Influence of porosity and microstructure on mechanical and corrosion properties of a selectively laser melted stainless steel. Journal of Alloys and Compounds, 831, pp. 154815.
[35] Hirata, T., Kimura, T. and Nakamoto, T. (2020). Effects of hot isostatic pressing and internal porosity on the performance of selective laser melted AlSi10Mg alloys, Materials Science and Engineering: A, 772, 138713.
[36] Liu, Y., Zhang, M., Shi, W., Ma, Y. and Yang, J. (2021). Study on performance optimization of 316L stainless steel parts by high-efficiency selective laser melting, Optics & Laser Technology, 138, pp. 106872.
[37] Ferro, P., Meneghello, R., Savio, G. and Berto, F. (2020). A modified volumetric energy density–based approach for porosity assessment in additive manufacturing process design, The International Journal of Advanced Manufacturing Technology, 110, pp. 1911-1921.
[38] De Souza, A.F., Al-Rubaie, K.S., Marques, S., Zluhan, B. and Santos, E.C. (2019). Effect of laser speed, layer thickness, and part position on the mechanical properties of maraging 300 parts manufactured by selective laser melting, Materials Science and Engineering: A, 767, pp. 138425.
[39] Abdel-Rahman, M.A., Hassan, S.E., El-Din, M.N., Azab, M.S., El-Belely, E.F., Alrefaey, H.M. and Elsakhawy, T. (2020). One-factor-at-a-time and response surface statistical designs for improved lactic acid production from beet molasses by Enterococcus hirae ds10, SN Applied Sciences, 2, pp. 1-14.
[40] Czitrom, V. (1999). One-factor-at-a-time versus designed experiments. The American Statistician, 53(2), pp. 126-131.
[41] Nor, N.M., Mohamed, M.S., Loh, T.C., Foo, H.L., Rahim, R.A., Tan, J.S. and Mohamad, R. (2017). Comparative analyses on medium optimization using one-factor-at-a-time, response surface methodology, and artificial neural network for lysine–methionine biosynthesis by Pediococcus pentosaceus RF-1. Biotechnology & Biotechnological Equipment, 31(5), pp. 935-947.
[42] Buyel, J.F. (2022). Statistical Designs to Improve Downstream Processing Downstream processing, In Recombinant Proteins in Plants: Methods and Protocols (pp. 295-310). New York, NY: Springer US.
[43] Wen, Y., Zhang, B., Liu, S., Cai, W., Wang, P., Lee, C.J.J., Ma, J. and Qu, X. (2020). A novel experimental method for in situ strain measurement during selective laser melting, Virtual and Physical Prototyping, 15(sup1), pp. 583-595.
[44] Waqar, S., Guo, K. and Sun, J. (2021). FEM analysis of thermal and residual stress profile in selective laser melting of 316L stainless steel, Journal of Manufacturing Processes, 66, pp. 81-100.
[45] Yin, X., Zhai, Q., Zhang, Q., Wang, K., Meng, L., Ma, Z., Chen, G., Wang, S. and Wang, L. (2021). Effect of tungsten particles on microstructure and properties of 316 L stainless steel manufactured by selective laser melting, Journal of Manufacturing Processes, 68, pp. 210-221.
[46] Hitzler, L., Hirsch, J., Heine, B., Merkel, M., Hall, W. and Öchsner, A. (2017). On the anisotropic mechanical properties of selective laser-melted stainless steel, Materials, 10(10), pp. 1136.
[47] Ren, B., Lu, D., Zhou, R., Li, Z. and Guan, J. (2019). Preparation and mechanical properties of selective laser melted H13 steel, Journal of Materials Research, 34(8), pp. 1415-1425.
[48] Kluczyński, J., Śnieżek, L., Grzelak, K., Oziębło, A., Perkowski, K., Torzewski, J., Szachogłuchowicz, I., Gocman, K., Wachowski, M. and Kania, B. (2020). Comparison of different heat treatment processes of selective laser melted 316L steel based on analysis of mechanical properties, Materials, 13(17), pp. 3805.
[49] Deng, Y., Mao, Z., Yang, N., Niu, X. and Lu, X. (2020). Collaborative optimization of density and surface roughness of 316L stainless steel in selective laser melting, Materials, 13(7), pp. 1601.
[50] Jiang, H.Z., Li, Z.Y., Feng, T., Wu, P.Y., Chen, Q.S., Feng, Y.L., Li, S.W., Gao, H. and Xu, H.J. (2019). Factor analysis of selective laser melting process parameters with normalised quantities and Taguchi method, Optics & Laser Technology, 119, pp. 105592.
[51] Li, J., Hu, J., Cao, L., Wang, S., Liu, H. and Zhou, Q. (2021a). Multi-objective process parameters optimization of SLM using the ensemble of metamodels, Journal of Manufacturing Processes, 68, pp. 198-209.
[52] Yadollahi, A., Shamsaei, N., Thompson, S. M., Elwany, A. and Bian, L. (2017). Effects of building orientation and heat treatment on fatigue behavior of selective laser melted 17-4 PH stainless steel, International Journal of Fatigue, 94, pp. 218-235.
[53] Mahmoudi, M., Elwany, A., Yadollahi, A., Thompson, S. M., Bian, L. and Shamsaei, N. (2017). Mechanical properties and microstructural characterization of selective laser melted 17-4 PH stainless steel, Rapid Prototyping Journal, 23(2), pp. 280-294.
[54] Linares, J.M., Chaves-Jacob, J., Lopez, Q. and Sprauel, J.M. (2022). Fatigue life optimization for 17-4Ph steel produced by selective laser melting, Rapid Prototyping Journal, 28(6), pp. 1182-1192.

[55] Vunnam, S., Saboo, A., Sudbrack, C. and Starr, T.L. (2019). Effect of powder chemical composition on the as-built microstructure of 17-4 PH stainless steel processed by selective laser melting, Additive Manufacturing, 30, pp. 100876.
[56] Ozsoy, A., Yasa, E., Keles, M. and Tureyen, E.B. (2021). Pulsed-mode Selective Laser Melting of 17-4 PH stainless steel: Effect of laser parameters on density and mechanical properties, Journal of Manufacturing Processes, 68, pp. 910-922.
[57] Leo, P., D'Ostuni, S., Perulli, P., Sastre, M.A.C., Fernández-Abia, A.I. and Barreiro, J. (2019). Analysis of microstructure and defects in 17-4 PH stainless steel sample manufactured by Selective Laser Melting, Procedia Manufacturing, 41, pp. 66-73.
[58] Garcia-Cabezon, C., Castro-Sastre, M.A., Fernandez-Abia, A.I., Rodriguez-Mendez, M.L. and Martin-Pedrosa, F. (2022). Microstructure–hardness–corrosion performance of 17–4 precipitation hardening stainless steels processed by selective laser melting in comparison with commercial alloy, Metals and Materials International, 28(11), pp. 2652-2667.
[59] Kartikeya Sarma, I., Selvaraj, N. and Kumar, A. (2023). Parametric investigation and characterization of 17-4 PH stainless steel parts fabricated by selective laser melting, Journal of Central South University, 30(3), pp. 855-870.
[60] Priya Sahadevan, Chithirai Pon Selvan, Amiya Bhaumik, and Avinash Lakshmikanthan (2023), Selective Laser Melting Parametric Optimization for Microhardness of 17-4 PH Stainless Steel. Journal of Mines, Metals and Fuels, 71(12), pp. 2512-2519. DOI: 10.18311/jmmf/2023/35128.
[61] Priya Sahadevan, Chithirai Pon Selvan, Amiya Bhaumik, and Avinash Lakshmikanthan (2023), Surface Roughness Optimization of Selective Laser Melting printed 17-4 PH Stainless Steel Parts, Journal of Mines, Metals and Fuels, 71(12), pp. 2405-2413. DOI: 10.18311/jmmf/2023/35123.
[62] Priya Sahadevan, Chithirai Pon Selvan, Manjunath Patel G C, Amiya Bhaumik (2023), Selective Laser Melting Process Parameter Optimization on Density and Corrosion Resistance of 17-4PH Stainless Steel, Archives of Foundry Engineering, ISSN (2299-2944), (4), pp. 105 – 116, DOI: 10.24425/afe.2023.146685.
[63] Simonelli, M.; Aboulkhair, N.T.; Cohen, P.; Murray, J.W.; Clare, A.T.; Tuck, C.; Hague, R.J.M. (2018). A comparison of Ti-6Al-4V in-situ alloying in Selective Laser Melting using simply-mixed and satellited powder blend feedstocks. Mater. Charact. 143, pp. 118–126.
[64] Avinash Lakshmikanthan, Srikanth Bontha, M Krishna, Praveennath G Koppad, T Ramprabhu (2019). Microstructure, mechanical and wear properties of the A357 composites reinforced with dual sized SiC particles. Journal of Alloys and Compounds-Elsevier, 786(25), pp. 570-580. DOI: 10.1016/j.jallcom.2019.01.382.-64.
[65] Zhang, M., Sun, C. N., Zhang, X., Goh, P. C., Wei, J., Hardacre, D. and Li, H. (2017). Fatigue and fracture behaviour of laser powder bed fusion stainless steel 316L: Influence of processing parameters. Materials Science and Engineering: A, 703, pp. 251-261.
[66] Manakari, V., Parande, G. and Gupta, M. (2016). Selective laser melting of magnesium and magnesium alloy powders: a review. Metals, 7(1), 2.
[67] Joo, H.M., Kim, W.C., Kim, Y.J., Jo, Y.C., Kang, M.G., Lee, J.Y., Kim, M.S., Kim, G.B., Kim, S.J. and Kim, D.H., 2023. Effect of laser power on the microstructure evolution and mechanical properties of 20MnCr5 low alloy steel produced by laser-based powder bed fusion. Metals and Materials International, 29(4), pp. 983-993.
[68] Hooper, P. A. (2018). Melt pool temperature and cooling rates in laser powder bed fusion. Additive Manufacturing, 22, pp. 548-559.
[69] Xie, D. and Dittmeyer, R. (2021). Correlations of laser scanning parameters and porous structure properties of permeable materials made by laser-beam powder-bed fusion. Additive Manufacturing, 47, 102261.
[70] Sheshadri R, Nagaraj M, Lakshmikanthan A, Chandrashekarappa MPG, Pimenov DY, Giasin K and Wojciechowski S. (2021). Experimental investigation of selective laser melting parameters for higher surface quality and microhardness properties: taguchi and super ranking concept approaches,Journal of materials research and technology, 14, pp. 2586-2600.
[71] Zhu, Y., Zou, J. and Yang, H. Y. (2018). Wear performance of metal parts fabricated by selective laser melting: a literature review. Journal of Zhejiang University-Science A, 19(2),pp. 95-110.
[72] Sagbas, B., Gencelli, G. and Sever, A. (2021). Effect of process parameters on tribological properties of Ti6Al4V surfaces manufactured by selective laser melting. Journal of Materials Engineering and Performance, 30, pp. 4966-4973. DOI: 10.1007/s11665-021-05573-y.
[73] Tian, Y., Tomus, D., Rometsch, P. and Wu, X. (2017). Influences of processing parameters on surface roughness of Hastelloy X produced by selective laser melting. Additive Manufacturing, 13, pp. 103-112. DOI: 10.1007/s11665-021-05573-y.
[74] Selvan, C. P., Girisha, L., Koti, V., Madgule, M., Davanageri, M. B., Lakshmikanthan, A. and Chandrashekarappa, M. P. G. (2023). Optimization of stir casting and drilling process parameters of hybrid composites. Journal of Alloys and Metallurgical Systems, 3, 100023.

[75] Patel GC, M., NB, P., HM, H. and Shettigar, A. K. (2022). Experimental analysis and optimization of plasma spray parameters on microhardness and wear loss of Mo-Ni-Cr coated super duplex stainless steel. Australian Journal of Mechanical Engineering, 20(5), pp. 1426-1438.

[76] Veeresh Nayak, C., Manjunath Patel, G.C., Ramesh, M.R., Desai, V., Samanta, S.K. (2020). Analysis and Optimization of Metal Injection Moulding Process. In: Gupta, K. (eds) Materials Forming, Machining and Post Processing. Materials Forming, Machining and Tribology. Springer, Cham. DOI: 10.1007/978-3-030-18854-2_2.

[77] Aripin, M.A., Sajuri, Z., Jamadon, N.H., Baghdadi, A.H., Syarif, J., Mohamed, I.F., Aziz, A.M. (2022). Effects of Build Orientations on Microstructure Evolution, Porosity Formation, and Mechanical Performance of Selective Laser Melted 17-4 PH Stainless Steel. Metals 12, 1968. DOI: 10.3390/met12111968.

[78] Zhao, Zhanyong, Hailin Wang, Pengcheng Huo, Peikang Bai, Wenbo Du, Xiaofeng Li, Jianmin Li, and Wei Zhang. 2022. "Effect of Solution Temperature on the Microstructure and Properties of 17-4PH High-Strength Steel Samples Formed by Selective Laser Melting" Metals 12(3), 425. DOI: 10.3390/met12030425.

[79] Ponnusamy, P.; Masood, S.H.; Ruan, D.; Palanisamy, S.; Rahman Rashid, R.A.; Mohamed, O.A. (2017). Mechanical performance of selective laser melted 17-4 PH stainless steel under compressive loading. In Proceedings of the 2017 International Solid Freeform Fabrication Symposium, Austin, TX, USA, pp. 321–331.

[80] Rohith, S., Mohan, N., Malik, V. (2023). Modelling and optimization of selective laser melting parameters using Taguchi and super ranking concept approaches. Int J Interact Des Manuf 17, 2415–2427. DOI: 10.1007/s12008-022-01011-y.